Atmospheric correction of SeaWiFS imagery for turbid coastal and inland waters

Kevin George Ruddick, Fabrice Ovidio, and Machteld Rijkeboer

The standard SeaWiFS atmospheric correction algorithm, designed for open ocean water, has been extended for use over turbid coastal and inland waters. Failure of the standard algorithm over turbid waters can be attributed to invalid assumptions of zero water-leaving radiance for the near-infrared bands at 765 and 865 nm. In the present study these assumptions are replaced by the assumptions of spatial homogeneity of the 765:865-nm ratios for aerosol reflectance and for water-leaving reflectance. These two ratios are imposed as calibration parameters after inspection of the Rayleigh-corrected reflectance scatterplot. The performance of the new algorithm is demonstrated for imagery of Belgian coastal waters and yields physically realistic water-leaving radiance spectra. A preliminary comparison with *in situ* radiance spectra for the Dutch Lake Markermeer shows significant improvement over the standard atmospheric correction algorithm. An analysis is made of the sensitivity of results to the choice of calibration parameters, and perspectives for application of the method to other sensors are briefly discussed. © 2000 Optical Society of America

OCIS codes: 010.1290, 010.4450, 120.0280.

1. Introduction

Ocean color remote sensing in the 1970's and 1980's focused primarily on open ocean case 1 waters, in which the variation of optical properties (absorption and scattering) is dominated by phytoplankton and associated material.[1] Applications include research in ocean dynamics and biological production. More recently, the importance of coastal zone and inland water applications, such as pollution monitoring, combined with a new generation of satellite sensors has led to a surge of interest in the inversion of remotely sensed data for case 2 waters. For such waters the optical properties of inorganic suspended matter and colored dissolved organic matter (CDOM, also called *gelbstoff*, yellow substance, or *gilvin*) must also be considered. The largest sources of error for chlorophyll retrieval in case 2 waters are generally attributed to the bio-optical model that relates water-leaving radiance (or reflectance) to the chlorophyll

K. G. Ruddick (k.ruddick@mumm.ac.be) and F. Ovidio are with the Management Unit of the Mathematical Models of the North Sea, 100 Gulledelle, B-1200 Brussels, Belgium. M. Rijkeboer is with the Institute for Environmental Studies, Free University of Amsterdam, De Boelelaan 1115, 1081 HV Amsterdam, The Netherlands.

concentration[2–7] and to treatment of aerosol reflectance in the atmospheric correction procedure.[8] Here only the latter problem is addressed.

Since, in the vast majority of cases, simultaneous *in situ* measurements of atmospheric optical properties are not available, the atmospheric correction of ocean color imagery usually relies on satellite-derived data alone. For open ocean waters it is common to assume zero water-leaving radiance at red or near-infrared wavelengths and a prescribed spectral form for aerosol reflectance, possibly with free calibration parameters. Thus aerosol reflectance is extrapolated from the red or near-infrared band(s) to shorter wavelengths. For the Coastal Zone Color Scanner (CZCS) such algorithms, assuming negligible water-leaving radiance at 670 nm,[9–11] have proved popular and have subsequently been extended to include multiple-scattering effects.[12] The standard Seaviewing Wide Field-of-view Sensor (SeaWiFS) atmospheric correction algorithm[13] adopts a similar approach, although it takes advantage of the two near-infrared bands (at 765 and 865 nm) for which water-leaving radiance is lower than at 670 nm. Whereas the CZCS algorithms were successful for relatively clear waters, the assumption of negligible water-leaving radiance at 670 nm breaks down for turbid waters, as found in case 1 waters with high chlorophyll concentrations or, even more seriously, in case 2 waters with high concentrations of inorganic suspended matter.

To overcome this shortcoming, a number of

authors[14–20] developed and applied atmospheric correction procedures for CZCS data whereby the water-leaving radiance at 670 nm is not assumed to be zero but is modeled from estimated values of the water-leaving radiance(s) at shorter wavelengths by use of empirical band ratio relations. In most of these schemes, which were developed mainly for case 1 waters, the set of water-leaving radiances is successively updated until the iterative procedure is considered as having converged. An alternative procedure[21] avoids the need for iteration by assuming a simple linear relationship between the water-leaving radiances at 550 and 670 nm. It is interesting to note that, although it was introduced primarily to reduce computer time and was considered somewhat artificial by its developers, such an approach has a sound theoretical basis for near-infrared bands, as we show in this paper.

Although they are clearly an improvement over the assumption of zero water-leaving radiance at 670 nm, all these algorithms are subject to calibration problems, especially in turbid coastal waters. The empirical relations between water-leaving radiances at any two visible bands cannot be expected to hold generally because of strong and uncorrelated variability in space and time of phytoplankton, inorganic suspended matter, and CDOM related to tidal resuspension, river plumes, etc. A more general treatment of CZCS atmospheric correction was achieved[8] by inversion of a coupled sea–atmosphere optical model to retrieve suspended matter, chlorophyll, *gelbstoff*, and aerosol reflectance from the four bands of CZCS Rayleigh-corrected radiances. In this approach a homogeneous Ångström exponent for aerosol reflectance was imposed from *in situ* measurements. With the advent of SeaWiFS, better atmospheric correction for turbid waters becomes possible because of the availability of two near-infrared bands as well as improved sensor calibration. In one paper[22] an atmospheric correction for case 2 waters was developed from a coupled sea–atmosphere model for SeaWiFS, including these two near-infrared bands. This algorithm iterates between the marine optical model, which has chlorophyll, suspended matter, and *gelbstoff* as unknowns, and the atmosphere model, which has variable aerosol type (defined by the relative proportions of continental and urban aerosols to maritime aerosols) and aerosol optical depth.

An iterative approach has also been adopted for a study of coastal waters in the Gulf of Mexico[23] in which the three SeaWiFS bands at 670, 765, and 865 nm are used. In that study, water-leaving radiances at 765 and 865 nm are estimated by extrapolation from the first estimate of the 670-nm water-leaving radiance (made by the standard SeaWiFS atmospheric correction) by use of a simple model of inherent optical properties. After this component is removed from the total radiance at 765 and 865 nm the atmospheric correction is reapplied to the other bands, including 670 nm, and the procedure is repeated until convergence. This algorithm is discussed further in Section 4 below.

As preparation for the atmospheric correction of Medium Resolution Imaging Spectrometer (MERIS) data, for which three near-infrared bands will be available at 705, 775, and 865 nm, a turbid water atmospheric correction has been developed for generation of standard MERIS case 2 water products.[24] In that algorithm the water reflectances at the three bands are connected by a model of the absorption and backscattering properties of sediment-laden waters, with suspended sediment concentration as a free parameter; the aerosol reflectances are assumed to obey a log-linear law. First the concentration of suspended sediment is estimated from an initial guess of spectrally flat aerosol reflectance, and the ratio of water reflectances is thus fixed. This leaves effectively three unknowns: the water reflectance at one wavelength, the coefficient that determines the aerosol reflectance spectral form, and the single-scattering aerosol reflectance at one wavelength. These three unknowns can be calculated from the three bands of Rayleigh-corrected reflectance data, and all relevant quantities can be derived, including the aerosol reflectance at all wavelengths, which is then used for the atmospheric correction of visible bands. In the present paper a similar approach is used, although further assumptions are required because only two near-infrared bands are available with SeaWiFS.

We describe a turbid water atmospheric correction for SeaWiFS data based on a simple extension of the standard algorithm.[13] The assumptions of zero water-leaving radiance for the near-infrared bands in that standard algorithm are replaced by the assumptions of homogeneity of the ratio of both aerosol reflectances and water-leaving reflectances at 765 and 865 nm over the region of interest. Crucially, the assumption of spatial homogeneity for the water-leaving reflectance ratio can be expected to be significantly more universally applicable than the previous empirical relationships for CZCS visible bands because of the simplicity of marine optical properties in the near infrared. Absorption is determined there almost entirely by pure seawater absorption, and backscattering has only weak spectral variation. Furthermore, with such assumptions the need for an iterative scheme is avoided because computation of the two unknown near-infrared water-leaving reflectances entails the simple solution of two simultaneous linear algebraic equations. The resultant algorithm is implemented in a two-step procedure, whereby calibration of the aerosol reflectance and water-leaving reflectance ratios for 765 and 865 nm are determined for each image from analysis of the scatterplot of Rayleigh-corrected reflectances at 765 and 865 nm.

In the following text, first the theoretical basis of the algorithm is described. Then the first test of the new algorithm is demonstrated for SeaWiFS imagery of Belgian coastal waters. Whereas the standard open ocean atmospheric correction algorithm fails completely for this region, which is known to be

highly turbid, the new algorithm gives qualitatively realistic spatial structures in water-leaving radiance maps as well as positive water-leaving radiance for all visible bands. A comparison is also made with *in situ* radiance measurements made for the Dutch Lake Markermeer. Finally, the practical implementation of the algorithm in the SeaWiFS Data Analysis System (SeaDAS) processing software is outlined, as is possible implementation for other sensors.

2. Method

A. Standard SeaWiFS Atmospheric Correction

Using throughout this section the theory and terminology of Gordon and Wang,[13] we define the reflectance ρ as

$$\rho = \pi L / F_0 \cos \theta_0, \qquad (1)$$

where L is the upward radiance in the given viewing direction, F_0 is the extraterrestrial solar irradiance, and θ_0 is the solar zenith angle. Then the total reflectance ρ_t, at a wavelength λ, measured at the top of the atmosphere can be decomposed into five components:

$$\rho_t(\lambda) = \rho_r(\lambda) + \rho_a(\lambda) + \rho_{ra}(\lambda) + T_v(\lambda)[\rho_w(\lambda) + \rho_{wc}(\lambda)], \qquad (2)$$

where ρ_r is the reflectance that results from multiple scattering by air molecules (Rayleigh scattering) in the absence of aerosols, ρ_a is the reflectance from multiple scattering by aerosols in the absence of air, ρ_{ra} is the reflectance from interaction between Rayleigh and aerosol scattering, ρ_{wc} is the reflectance from the air–sea interface, ρ_w is the water-leaving reflectance, and T_v is the viewing diffuse atmospheric transmittance from sea to sensor. With the normalization [Eq. (1)], addition of reflectances as in Eq. (2) is as trivial as addition of radiances. However, we note that ρ_w will vary proportionally with the sun–sea atmospheric transmittance T_0, all other factors being equal. An alternative normalization, used by the standard SeaWiFS products data set, is provided by the normalized water-leaving radiance, $[L_w]_N$, defined by[25,26]

$$[L_w]_N = \frac{L_w}{T_0 \cos \theta_0}, \qquad (3)$$

which is used here only for the presentation of imagery.

The Rayleigh scattering component ρ_r is calculated directly from the illumination and viewing geometry (sun and sensor zenith and azimuth angles) by use of lookup tables but with a correction for atmospheric pressure if available as ancillary data. The component ρ_{wc}, which is assumed to be dominated by reflectance from whitecaps (tilting the sensor avoids sun glitter), is calculated from an empirical wind speed formulation[27] but reduced by a factor of 0.25 as implemented in the SeaWiFS reprocessing announced in August 1998. Subtraction of these two

components gives the Rayleigh-corrected reflectance, ρ_c, which is defined as

$$\rho_c(\lambda) = \rho_t(\lambda) - \rho_r(\lambda) - T_v(\lambda)\rho_{wc}(\lambda)$$
$$= \rho_a(\lambda) + \rho_{ra}(\lambda) + T_v(\lambda)\rho_w(\lambda). \qquad (4)$$

It is assumed that the effects of ozone and (for the SeaWiFS 765-nm band) of oxygen on atmospheric transmittance can be treated separately by decomposition of T_v and T_0 according to

$$T_v = t_{v(a+r)}t_{v(oz)}t_{v(O_2)}, \qquad (5)$$

$$T_0 = t_{0(a+r)}t_{0(oz)}t_{0(O_2)}, \qquad (6)$$

where $t_{v(a+r)}$, $t_{v(oz)}$, $t_{v(O_2)}$, etc. are the atmospheric transmittance factors for aerosol and Rayleigh effects[28,29] for ozone absorption and for oxygen absorption,[30] respectively. To model aerosol and water-leaving reflectances independently of ozone content Eq. (4) is renormalized by division by the two-way ozone and oxygen transmittances. This gives

$$\rho_c'(\lambda) = \rho_a'(\lambda) + \rho_{ra}'(\lambda) + t_{v*}(\lambda)\rho_w(\lambda), \qquad (7)$$

where

$$\rho' = \frac{\rho}{t_{v(oz)}t_{v(O_2)}t_{0(oz)}t_{0(O_2)}} \qquad (8)$$

and t_{v*} is the viewing atmospheric transmittance corrected for two-way ozone and, for band 7, oxygen absorption:

$$t_{v*} = \frac{T_v}{t_{v(oz)}t_{v(O_2)}t_{0(oz)}t_{0(O_2)}} = \frac{t_{v(a+r)}t_{0(a+r)}}{T_0}. \qquad (9)$$

To simplify the notation we drop the prime symbols in the following text and write the total multiple-scattering aerosol reflectance as ρ_{am}, which is defined as

$$\rho_{am}(\lambda) = \rho_a(\lambda) + \rho_{ra}(\lambda). \qquad (10)$$

It is necessary to calculate this multiple-scattering aerosol reflectance to obtain finally the desired ρ_w for the visible SeaWiFS bands for subsequent use in a bio-optical model. Doing so requires further knowledge or assumptions regarding the spectral form of ρ_{am} as well as the value of this term for a single wavelength. The standard SeaWiFS algorithm[13] assumes zero ρ_w for $\lambda_7 = 765$ nm and $\lambda_8 = 865$ nm, giving

$$\rho_{am}^{(7)} = \rho_c^{(7)}, \qquad (11)$$

$$\rho_{am}^{(8)} = \rho_c^{(8)}, \qquad (12)$$

where the notation $\rho_x^{(i)}$ represents a reflectance at SeaWiFS band i with wavelength λ_i. These multiple-scattering aerosol reflectances are then used to choose the most appropriate aerosol model from a family of N aerosol models, corresponding to typical particle size distributions (e.g., maritime, tropospheric, coastal, and urban) and discrete values of relative humidity (e.g., RH of 50%, 70%, 90%, 99%).

For each aerosol model ($I = 1 \ldots N$), lookup tables have been calculated for the ratio $\varepsilon_{s(I)}^{(i,j)}$ of single-scattering aerosol reflectance $\rho_{as}^{(i)}$ for any two bands (i, j) as defined by

$$\varepsilon_{s(I)}^{(i,j)} \equiv \frac{\rho_{as}^{(i)}}{\rho_{as}^{(j)}}. \qquad (13)$$

This ratio is calculated individually for each pixel because of the dependence on viewing and illumination geometry (this dependence on sun and satellite zenith and azimuth angles is dropped here and in what follows for notational convenience). Similarly, lookup tables derived from atmospheric model simulations are used to define the monotonic near-linear relationship (and its inverse) between ρ_{am} and the single-scattering aerosol reflectance ρ_{as}:

$$\rho_{am}^{(i)} = f^I[\rho_{as}^{(i)}], \qquad (14)$$

$$\rho_{as}^{(i)} = g^I[\rho_{am}^{(i)}]. \qquad (15)$$

For each candidate aerosol model $\rho_{as(I)}^{(7)}$ and $\rho_{as(I)}^{(8)}$ are calculated for each pixel from Eq. (15), and the corresponding retrieved single-scattering aerosol reflectance ratio $\varepsilon_{*s(I)}^{(7,8)}$ is calculated from Eq. (13). Comparing these $\varepsilon_{*s(I)}^{(7,8)}$ with the theoretical tabulated $\varepsilon_{s(I)}^{(7,8)}$ determines the best-fit aerosol model (in fact, this model is a weighted interpolation between the two best-fitting models, thus giving a continuous rather than a discrete range of candidate models). Thus with the spectral form of the single-scattering aerosol reflectance determined, the magnitude of ρ_{as}, and hence of ρ_{am}, can be calculated for all wavelengths from $\rho_{as}^{(8)}$. Finally, the aerosol and aerosol–Rayleigh scattering components are removed from the Rayleigh-corrected reflectance for the six visible bands, λ_{1-6}, and the result is divided by the atmospheric transmittance to yield the full set of eight water-leaving reflectances $\rho_w^{(1-8)}$, which include, implicitly, zero values for $\rho_w^{(7)}$ and $\rho_w^{(8)}$. The steps of this algorithm are summarized thus:

(1) Enter the atmospheric correction routine with data for Rayleigh-corrected reflectances $\rho_c^{(7)}$ and $\rho_c^{(8)}$.

(2) Set multiple-scattering aerosol reflectances $\rho_{am}^{(7)}$ and $\rho_{am}^{(8)}$ equal to the Rayleigh-corrected reflectances.

(3) Calculate the corresponding single-scattering aerosol reflectances $\rho_{as(I)}^{(7)}$ and $\rho_{as(I)}^{(8)}$ for each candidate aerosol model from Eq. (15) and hence $\varepsilon_{*s(I)}^{(7,8)}$ from Eq. (13).

(4) Select the best two aerosol models by comparing the retrieved $\varepsilon_{*s(I)}^{(7,8)}$ with the theoretical $\varepsilon_{s(I)}^{(7,8)}$ and determine the interpolation ratio between them.

(5) For the optimal aerosol model use the tabulated $\varepsilon_s^{(1-6,8)}$ to obtain $\rho_{as}^{(1-6)}$ and then $\rho_{am}^{(1-6)}$.

(6) Remove $\rho_{am}^{(1-6)}$ from $\rho_c^{(1-6)}$ and divide by the atmospheric transmittance that corresponds to the best aerosol model to return $\rho_w^{(1-6)}$.

This procedure is carried out on a pixel-by-pixel basis, except that, to save computing time, the best-fit aerosol model can be assumed constant for a few

continuous pixels along a scan line. This corresponds to allowing a different aerosol type and aerosol concentration (or optical thickness) at every pixel.

B. Extension of the Standard SeaWiFS Atmospheric Correction to Turbid Waters

To clarify the number of assumptions needed for an extension of this atmospheric correction procedure to turbid waters it is useful to summarize the available relations and the unknown quantities involved.

Thus, for the eight-band SeaWiFS band set, eight equations are given by

$$\rho_{am}^{(i)} + t_{v*}^{(i)}\rho_w^{(i)} = \rho_c^{(i)}, \qquad i = 1 \ldots 8, \qquad (16)$$

where $\rho_c^{(i)}$ is given by the image data for each pixel and $t_{v*}^{(i)}$ is known from the viewing geometry and the choice of aerosol model. Seven further relations are given by the aerosol model:

$$\varepsilon_{s(I)}^{(i,8)} = \frac{g^I[\rho_{am}^{(i)}]}{g^I[\rho_{am}^{(8)}]}, \qquad (17)$$

where $\varepsilon_{s(I)}^{(i,8)}$ and g^I are tabulated. The unknowns comprise the eight aerosol reflectances $\rho_{am}^{(1-8)}$, the eight water-leaving reflectances $\rho_w^{(1-8)}$, and the best-fit aerosol model index, $I = I_0$. In the standard atmospheric correction procedure the two further equations used to close the system are $\rho_w^{(7)} = 0$ and $\rho_w^{(8)} = 0$. However, it is clear from *in situ* measurements[23,31,32] that such an approximation is not valid for highly turbid coastal waters [see also the discussion of Fig. 1 (below)]. To extend this algorithm to turbid waters it is necessary to replace these two assumptions with two other relations. In this paper the following two assumptions are used:

(1) The ratio of multiple-scattering aerosols and aerosol-Rayleigh reflectances at 765 and 865 nm is assumed to be spatially homogeneous, at least over the subscene of interest:

$$\frac{\rho_{am}^{(7)}}{\rho_{am}^{(8)}} \equiv \varepsilon_m^{(7,8)}, \qquad (18)$$

where this ratio $\varepsilon_m^{(7,8)}$ is considered a calibration parameter to be fixed for each image.

(2) The ratio of water-leaving reflectances normalized by the sun–sea atmospheric transmittance at 765 and 865 nm is assumed to be spatially homogeneous, at least over the subscene of interest:

$$\alpha \equiv \frac{\rho_w^{(7)}/T_0^7}{\rho_w^{(8)}/T_0^8}, \qquad (19)$$

where this ratio α is considered a calibration parameter to be fixed for each image, although a default value of rather universal applicability can also be used, as we explain below.

A discussion of the range of validity of each of these assumptions can be found in the following sections.

We now use the new assumptions [Eqs. (18) and (19)] to extend for turbid waters the standard algo-

rithm described in Subsection 2.A. Equations (9) and (19) yield

$$t_{v*}^{(7)}\rho_w^{(7)} = \frac{t_{v(a+r)}^{(7)}t_{0(a+r)}^{(7)}}{T_0^{(7)}}\,\rho_w^{(7)} = t_{v(a+r)}^{(7)}t_{0(a+r)}^{(7)}\alpha\,\frac{\rho_w^{(8)}}{T_0^{(8)}} = \alpha\gamma t_{v*}^{(8)}\rho_w^{(8)},$$

(20)

where the band 7:8 ratio of atmospheric transmittances from Rayleigh and aerosol effects is given by

$$\gamma = \frac{t_{v(a+r)}^{(7)}t_{0(a+r)}^{(7)}}{t_{v(a+r)}^{(8)}t_{0(a+r)}^{(8)}}.$$

(21)

The four atmospheric transmittance factors in Eq. (21) depend on viewing and illumination geometry and, albeit weakly, on aerosol optical thickness and aerosol type. Thus it is not possible to calculate them until after the aerosol model and optical thickness have been deduced, and they must be considered unknowns at this stage of the algorithm. However, using the diffuse transmittance tables generated from radiative transfer computations for the ocean–atmosphere system and available within SeaDAS for processing of SeaWiFS data, we find that the wavelength variation of these factors between 765 and 865 nm is small, and the ratio γ is found to lie between 0.98 and 1.00 for typical aerosol optical thicknesses and sun and viewing angles for all coastal aerosol models. Thus, in what follows, γ will be taken equal to 1.0.

Using Eqs. (18) and (20), we can rewrite Eq. (16) for bands 7 and 8 as

$$\varepsilon_m^{(7,8)}\rho_{am}^{(8)} + \alpha t_{v*}^{(8)}\rho_w^{(8)} = \rho_c^{(7)},$$

(22)

$$\rho_{am}^{(8)} + t_{v*}^{(8)}\rho_w^{(8)} = \rho_c^{(8)},$$

(23)

which can be solved simply to give

$$\rho_{am}^{(8)} = \frac{\alpha\rho_c^{(8)} - \rho_c^{(7)}}{\alpha - \varepsilon_m^{(7,8)}},$$

(24)

$$t_{v*}^{(8)}\rho_w^{(8)} = \frac{\rho_c^{(7)} - \varepsilon_m^{(7,8)}\rho_c^{(8)}}{\alpha - \varepsilon_m^{(7,8)}},$$

(25)

$$\rho_{am}^{(7)} = \varepsilon_m^{(7,8)}\left[\frac{\alpha\rho_c^{(8)} - \rho_c^{(7)}}{\alpha - \varepsilon_m^{(7,8)}}\right],$$

(26)

$$t_{v*}^{(7)}\rho_w^{(7)} = \alpha\left[\frac{\rho_c^{(7)} - \varepsilon_m^{(7,8)}\rho_c^{(8)}}{\alpha - \varepsilon_m^{(7,8)}}\right].$$

(27)

These aerosol reflectances $\rho_{am}^{(7)}$ and $\rho_{am}^{(8)}$ can then be passed to the standard algorithm [instead of $\rho_c^{(7)}$ and $\rho_c^{(8)}$] to complete the processing: derivation of $\rho_{as(I)}^{(7)}$ and $\rho_{as(I)}^{(8)}$, and hence of $\varepsilon_{*s(I)}^{(7,8)}$, and the best-fit aerosol model I_0, etc. Although the best-fit aerosol model will then tend to be almost spatially homogeneous, with $\varepsilon_{s(I_0)}^{(7,8)}$ almost equal to the calibration parameter $\varepsilon_m^{(7,8)}$ and strictly equal in the single-scattering limit, the aerosol concentration (or equivalently the aerosol optical thickness or the aerosol reflectance at 865 nm) is still allowed to vary freely over the image.

The new turbid water atmospheric correction algorithm can be summarized thus:

(1) Enter the atmospheric correction routine to produce a scatter plot of Rayleigh-corrected reflectances $\rho_c^{(7)}$ and $\rho_c^{(8)}$ for the region of study. Select the calibration parameters α and $\varepsilon_m^{(7,8)}$ on the basis of this scatter plot or from *in situ* measurements or from default values.

(2) Reenter the atmospheric correction routine with data for Rayleigh-corrected reflectances $\rho_c^{(7)}$ and $\rho_c^{(8)}$ and use Eqs. (26) and (24) to deduce $\rho_{am}^{(7)}$ and $\rho_{am}^{(8)}$, taking account of nonzero water-leaving reflectances.

(3)–(6) Continue as for the standard algorithm.

C. Calibration of the Aerosol Reflectance Ratio

The calibration parameter $\varepsilon_m^{(7,8)}$ is evaluated from inspection of the band 7:8 Rayleigh-corrected scattergram. An example is shown in Fig. 4 below and discussed there. The assumption of spatial homogeneity of the ratio of multiple-scattering aerosol reflectance at two suitably chosen bands (preferably red or near infrared) was made previously in many studies[9,20,26,33] with both the CZCS and the Advanced Very High Resolution Radiometer (AVHRR). This assumption is based on the fact that, although aerosol concentration can vary considerably over small space scales, the aerosol type (or particle size distribution) can be expected to vary only weakly in space. A number of shortcomings in this assumption have been noted[34] in the context of pigment concentration estimation for case 1 waters. However, provided that the region over which spatial homogeneity is assumed is fairly small (e.g., 200 km), the most serious violations of the assumption of spatial homogeneity of multiple-scattering aerosol reflectance probably occur when atmospheric fronts or strong aerosol sources (e.g., from land-based industry) are present within the region. The assumption is somewhat less applicable in a multiple-scattering perspective because some dependence of the reflectance ratio on viewing angle can be expected: However, again, provided that the subimages considered are relatively small, such effects are likely to be second order.

D. Calibration of the Water-Leaving Reflectance Ratio

In practice, the calibration parameter α has been set equal to a default value of 1.72 for all images. One can obtain a theoretical basis for the assumption of spatial homogeneity of the ratio of water-leaving reflectances at 765 and 865 nm and an estimation of this default value by considering an ocean color model. Here a first-order estimate of this ratio is made by use of a greatly simplified model. We examine each of the major assumptions and approximations in turn in Appendix B to assess the sensitivity of this ratio to second-order effects such as wavelength dependency of the backscatter coefficient. To obtain a first estimate of the ratio of water-leaving reflectances at 765 and 865 nm normalized by sun–sea atmospheric transmittance we make the following assumptions:

The water-leaving reflectance ρ_w is related to the subsurface irradiance reflectance R by use of a marine reflectance model[26] that however neglects the internal reflectance of the upwelling radiance field by the sea surface:

$$R = \frac{1}{M}\frac{Q}{\pi}\frac{\rho_w}{T_0}, \qquad (28)$$

where M is a constant (≈ 0.523) that accounts for refraction and Fresnel internal reflection at the air–sea interface and Q is the ratio of upwelling radiance to the upwelling irradiance and is equal to π for a Lambertian surface.

The subsurface irradiance reflectance can in turn be related to the inherent optical properties[35]—the absorption coefficient a and the backscatter coefficient b_b—of the water and its constituents by the model

$$\frac{R}{Q} = l_1 \frac{b_b}{a}, \qquad (29)$$

where $l_1 = 0.0949$.[26] In this expression terms of order $(b_b/a)^2$ have been neglected in view of the small ($\ll 0.1$) near-infrared reflectances encountered in this context.

In the near infrared, absorption by CDOM, phytoplankton-related pigments, and other suspended particulate matter is assumed to be negligible compared with absorption by pure water,[36] denoted $a_w(\lambda)$:

$$a(\lambda) = a_w(\lambda). \qquad (30)$$

The backscatter coefficient is assumed to be independent of wavelength for the wavelength range considered and is denoted b_{b0}. Thus

$$b_b(\lambda) = b_{b0}. \qquad (31)$$

Combining these expressions gives

$$\frac{\rho_w(\lambda)}{T_0(\lambda)} = Ml_1\pi\frac{b_{b0}}{a_w(\lambda)}. \qquad (32)$$

Thus, in the limit of these approximations, wavelength variation of water-leaving reflectance is determined entirely by the wavelength dependency of pure water absorption, which can be expected to be rather constant for all regions and times. Thus for a delta-function sensor response the ratio of water-leaving reflectances at the two SeaWiFS near-infrared wavelengths is given by

$$\alpha = \frac{\rho_w^{(7)}/T_0^{(7)}}{\rho_w^{(8)}/T_0^{(8)}} = \frac{a_w^{(8)}}{a_w^{(7)}}, \qquad (33)$$

where $a_w^{(i)}$ represents the pure water absorption coefficient at wavelength λ_i. For $\lambda_7 = 765$ nm and $\lambda_8 = 865$ nm, the data of Palmer and Williams[36] give

$$\alpha = \frac{4.436 \text{ m}^{-1}}{2.586 \text{ m}^{-1}} = 1.72. \qquad (34)$$

E. Estimation of Errors

The effects of the key assumptions of spatial homogeneity of the band 7:8 ratios of aerosol path and water-leaving reflectance on the accuracy of derived water-leaving reflectances are analyzed in this subsection. Other possible sources of error (sensor calibration, whitecap correction, aerosol model, etc.) are not considered because the objective here is to isolate the errors associated with the turbid water component of the atmospheric correction procedure and thus to provide a basis for future improvement with other sensors. As derived in Appendix A, the error in water-leaving reflectance, $\Delta\rho_w^{(i)}$, associated with an uncertainty in estimation of $\varepsilon_m^{(7,8)}$ and α (arising from spatial variability or other factors) of $\Delta\varepsilon_m^{(7,8)}$ and $\Delta\alpha$ is given by

$$\Delta\rho_w^{(i)} = -\frac{1}{t_{v*}^{(i)}}\varepsilon_m^{(i,8)}\left[K^{(i)}\rho_{am}^{(8)}\Delta\varepsilon_m^{(7,8)} + \frac{t_{v*}^{(8)}}{\alpha - \varepsilon_m^{(7,8)}}\rho_w^{(8)}\Delta\alpha\right]. \qquad (35)$$

We evaluate this expression in Table 1, using values typical of the southern North Sea: $t_{v*}^{(i)} = 1$ and $\varepsilon_m^{(7,8)} = 1.10$ with $\rho_{am}^{(8)}$ varying from 0.005 (clear atmosphere) to 0.015 (turbid atmosphere) and $\rho_w^{(8)}$ varying from 0.001 (clear water) to 0.020 (turbid water). Practical experience with SeaWiFS imagery of this region suggests a typical error of $\Delta\varepsilon_m^{(7,8)} = 0.05$, and theoretical considerations described in detail in Appendix B give a typical error of $\Delta\alpha = 0.22$ (associated with linear spectral variation of particulate backscatter).

For turbid waters Table 1 shows that the errors for the assumptions of this turbid water algorithm are smaller than $\rho_w^{(8)}$ at all wavelengths, and, because $\rho_w^{(i)}$ is generally an order of magnitude larger than $\rho_w^{(8)}$ except for the 412-nm band, this result is encouraging especially when one considers that the standard algorithm fails for all bands in such conditions. However, we note that the errors associated with unresolved variations in $\varepsilon_m^{(7,8)}$ can become important in clear water with a turbid atmosphere. Within the constraint of the limited spectral information available from SeaWiFS it is difficult to design a robust algorithm that will give good performance for turbid waters while retaining the advantage of a pixel-by-pixel approach for clear waters.

F. Practical Considerations

The turbid water atmospheric correction algorithm described is highly compatible with the SeaDAS software,[37] which is the standard for processing of SeaWiFS imagery. The extra calculations performed amount to merely 15 extra lines of code. The extra code necessary for passing of arguments, including the calibration parameters, and for outputting Rayleigh-corrected reflectances consists of a few hundred lines.

With a view to making the whole image-processing chain operational in a region-specific service, a high degree of automation of the procedure has been achieved. Thus, standard operations such as cropping to a predefined region, cloud and land masking, level 2 file generation, and Rayleigh-corrected reflectance scatterplot generation can all be performed in

Table 1. Estimation of Errors Associated with Turbid Water Atmospheric Correction Assumptions from Eq. (A8) with $t_v^{(i)} = 1$ and $\varepsilon_m^{(7,8)} = 1.10$ and Typical Values of $\rho_{am}^{(8)} = 0.005$ for a Clear Atmosphere and $\rho_{am}^{(8)} = 0.015$ for a Turbid Atmosphere, $\rho_w^{(8)} = 0.001$ for Clear Water and $\rho_w^{(8)} = 0.020$ for Turbid Water, $\Delta\varepsilon_m^{(7,8)} = 0.05$, and $\Delta\alpha = 0.13 \times 1.72$

				$\Delta\rho_w^{(i)}$			
				Clear Atmosphere, $\rho_{am}^{(8)} = 0.005$		Turbid Atmosphere, $\rho_{am}^{(8)} = 0.015$	
Band (i)	Wavelength (nm)	$K^{(i)}$	$\varepsilon_m^{(i,8)}$	Clear Water, $\rho_w^{(8)} = 0.001$	Turbid Water, $\rho_w^{(8)} = 0.020$	Clear Water, $\rho_w^{(8)} = 0.001$	Turbid Water, $\rho_w^{(8)} = 0.020$
1	412	5.73	1.54	0.0028	0.0133	0.0072	0.0177
2	443	5.45	1.50	0.0026	0.0128	0.0066	0.0169
3	490	5.02	1.43	0.0023	0.0121	0.0059	0.0157
4	510	4.84	1.40	0.0022	0.0118	0.0056	0.0152
5	555	4.43	1.34	0.0020	0.0112	0.0050	0.0142
6	670	3.39	1.20	0.0015	0.0097	0.0035	0.0117
7	765	2.52	1.10	0.0011	0.0086	0.0025	0.0100
8	865	1.61	1.00	0.0008	0.0076	0.0016	0.0084

SeaDAS batch mode. For the whole chain from receipt of a level 1A image from the Distributed Active Archive Center of the Goddard Space Flight Center to production of maps of subsurface irradiance reflectance, human intervention is required only to improve the georeferencing by simple translation and to assess the values of the calibration parameter $\varepsilon_m^{(7,8)}$ by inspection of the Rayleigh-corrected scatterplots. Thus, once the system is set up for a specified region, the marginal cost of image processing is of the order of 1 h per image. However, a more detailed assessment of image quality based on expert analysis of level 1A imagery (identification of unfavorable atmospheric conditions, haze, etc.), level 2 error and warning flags, knowledge of local conditions, assimilation of *in situ* data, etc. is clearly still advisable.

3. Results

A. SeaWiFS Imagery of Belgian Coastal Waters

In this section we describe tests of the new atmospheric correction algorithm for SeaWiFS imagery of Belgian coastal waters in the southern North Sea. This region is a relatively shallow area (10–40-m water depth) where strong semidiurnal tides with current amplitude of $\sim 1 \text{ ms}^{-1}$ combine with frequent strong winds to cause relatively high concentrations of suspended particulate matter (SPM) (e.g., 1–200 g m^{-3}) by means of resuspension of bottom sediments.[38] Regarding the optical properties of the region, there is strong absorption in the blue from CDOM that is thought to be of terrestrial origin, e.g., a CDOM absorption coefficient at 400 nm of 0.1–2 m^{-1}, as well as absorption from detritus and phytoplankton pigments both in the blue and near the 670-nm chlorophyll absorption band.[39] Chlorophyll concentrations range from 0.01 to ~ 50.0 mg m^{-3} during the spring phytoplankton bloom.[40]

The SeaWiFS image taken at 12:15 UTC on 28 October 1997 has been selected as one of the best cloud-free images of the Belgian coastal zone during the first few months of SeaWiFS operation. For the region of interest the sun and viewing zenith angles are 65° and 35°, respectively, and the relative azimuth angle between sun and sensor is 50°. At the time of this image wind speed at 10 m above sea level was ~ 7 m/s, and air temperature was recorded as 8 °C with a subzero dew-point temperature (data from the Royal Netherlands Meteorological Institute monthly bulletin). The image was processed with SeaDAS software version 3.2 update 3. First the level 1A (raw digital counts) image was cropped to the southern North Sea and reprocessed to level 1A to account for the first global reprocessing of SeaWiFS data.[41] Then the automatic georeferencing based on navigational data was improved by a simple manually calculated translation of the image over a few kilometers. Radiometric calibration is described by McClain *et al.*[42] At this stage it is interesting to inspect the 765-nm top-of-atmosphere radiance (level 1B) image. As shown in Fig. 1, although much of the water area appears uniformly dark, certain spatial structures, which are collocated with areas known to be highly turbid such as submerged sandbanks, can be seen. As an example, the Flemish banks can be clearly distinguished; this is a region where SPM concentrations reach 50–200 g m^{-3} but with water depth sufficient for bottom reflection to be negligible at the sea surface. Although it is rather qualitative, this observation already suggests that the assumption in the standard SeaWiFS atmospheric correction algorithm of zero water-leaving radiance at 765 nm is not valid for this region.

1. Tests with the Standard Atmospheric Correction Algorithm

This image is then processed to level 2 normalized water-leaving radiances by use of the standard SeaWiFS atmospheric correction algorithm but with the 865-nm albedo threshold for cloud–ice detection increased from the default 1.1% to 2% to avoid erroneous flagging of highly turbid water as clouds. This change has not significantly degraded cloud detection for imagery of Belgian coastal waters. However, we note that one-band albedo threshold tests for cloud detection[43] may need to be enhanced for turbid water applications because the assumption of low near-
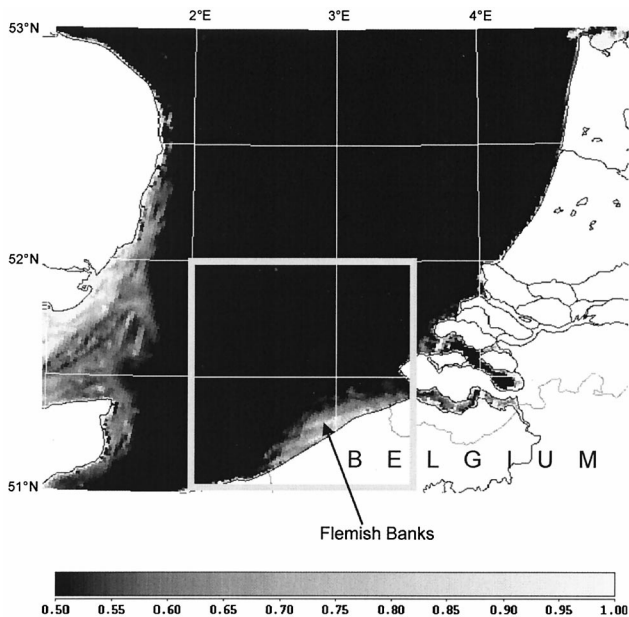
Fig. 1. Top-of-atmosphere radiance (mW cm^{-2} μm^{-1} sr^{-1}) at 765 nm for the SeaWiFS image taken 28 October 1997, 12:15 UTC. The heavily outlined box is the subregion, defined by top-right and bottom-left corners at (52°N, 3.5°E) and (51°N, 2°E), used subsequently for calibration of the turbid water atmospheric correction algorithm.

infrared water-leaving radiance is no longer valid. Although it is outside the scope of this paper, it is conceivable that a one-albedo threshold test could be combined with a near-infrared band ratio test because turbid water and clouds or dusts will have widely different values for $\rho_c^{(7)}/\rho_c^{(8)}$ at high reflectances.

The resultant normalized water-leaving radiances at 443 and 670 nm are shown in Figs. 2 and 3, respectively, where the white areas denote complete failure of the algorithm. For these areas the single-scattering aerosol reflectance ratio $\varepsilon_s^{(7,8)}$ deduced from the image data by the standard atmospheric correction reaches a value of 1.6, causing error flagging of the algorithm and, if calculations are allowed to continue, negative water-leaving radiances for the lowest wavelengths. At 412 nm, water-leaving radiances (not shown) are negative except for a handful of pixels.

2. Tests with Turbid Water Atmospheric Algorithm Correction

The turbid water atmospheric correction algorithm is applied in two stages. First a modified version of the SeaDAS level 2 product generation code is used to output the Rayleigh-corrected reflectances at 765 and 865 nm for all water pixels bounded by the box with top-right and bottom-left corners at (52 °N, 3.5 °E) and (51 °N, 2 °E) that is outlined in Fig. 1. The scatterplot of these reflectances is then plotted and inspected subjectively for calibration of the parameters $\varepsilon_m^{(7,8)}$ and α. As shown in Fig. 4, this scatterplot shows a dense cluster of points with low Rayleigh-corrected reflectances (e.g., from 0.002 to 0.01 for 765
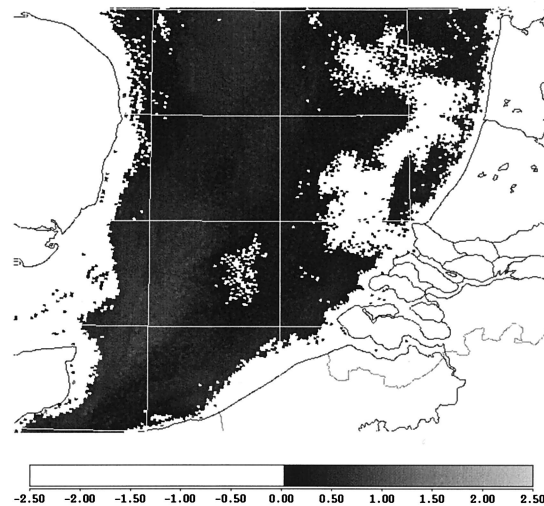

Fig. 2. Normalized water-leaving radiance (mW cm^{-2} μm^{-1} sr^{-1}) for the SeaWiFS image taken 28 October 1997, 12:15 UTC, at 443 nm after the standard atmospheric correction.

nm) where the relation between 765- and 865-reflectances is almost linear with a slope slightly smaller than 1. These points correspond to fairly clear water where the Rayleigh-corrected reflectance is dominated by aerosol reflectance. The nearly linear relation supports a hypothesis of spatial homogeneity of aerosol type (or reflectance ratio), although the range of reflectances encountered indicates considerable variability of aerosol concentration. The maximal slope of this relation is given theoretically by $\rho_c^{(7)}/\rho_c^{(8)} = \varepsilon_m^{(7,8)}$. For higher reflectance (e.g., from 0.02 to 0.05 for 765 nm) there is still a strong correlation between the two bands, although the slope of the relation has clearly changed. These points cor-
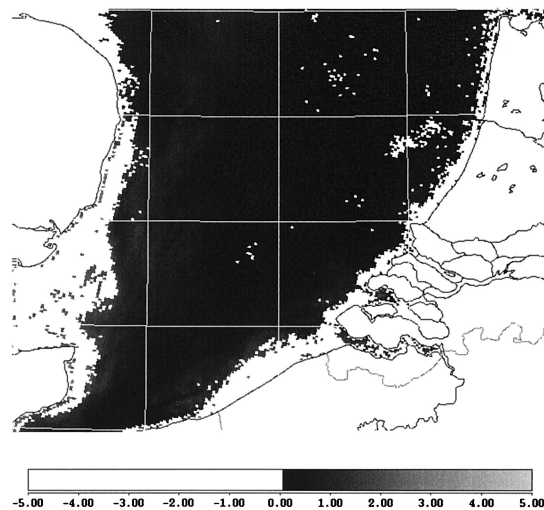

Fig. 3. Normalized water-leaving radiance (mW cm^{-2} μm^{-1} sr^{-1}) for the SeaWiFS image taken 28 October 1997, 12:15 UTC, at 670 nm after the standard atmospheric correction.
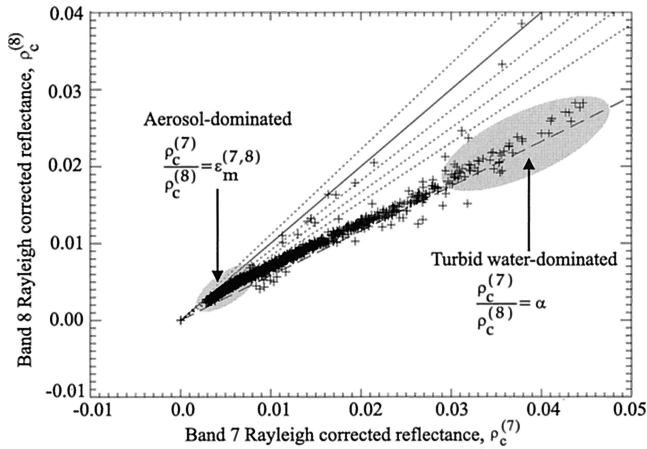
Fig. 4. Scatterplot of Rayleigh-corrected reflectances at 765 and 865 nm for the subregion outlined in Fig. 1 of the SeaWiFS image taken 28 October 1997, 12:15 UTC. The superimposed straight lines correspond to $\rho_c^{(7)}/\rho_c^{(8)} = 1$ (solid line); $= 0.09, 1.10, 1.20$ (short-dashed lines); $= 1.72$ (long-dashed line).

Fig. 5. Normalized water-leaving radiance (mW cm^{-2} μm^{-1} sr^{-1}) for the SeaWiFS image taken 28 October 1997, 12:15 UTC, at 443 nm after the turbid water atmospheric correction.

respond to highly turbid water where the Rayleigh-corrected reflectance is dominated by water-leaving reflectance, which gives theoretically a slope $\rho_c^{(7)}/\rho_c^{(8)} = \alpha$. The reason some data points lie well outside the dominant cluster on this scatterplot is not known, although partial land–sea pixels and partially cloudy pixels are potential causes, as are possible spatial inhomogeneities in aerosol type and suspended sediment type. Points that lie outside the region enclosed by $\varepsilon_m^{(7,8)} < \rho_c^{(7)}/\rho_c^{(8)} < \alpha$ will fail even the turbid water atmospheric correction but are sufficiently rare in this image as to pose no serious problems in subsequent image quality. On the basis of this scatterplot the calibration parameter $\varepsilon_m^{(7,8)} = 1.05$ was chosen for the subsequent turbid water atmospheric correction. The general calibration $\alpha = 1.72$ was chosen and is consistent with this scatterplot.

In the second stage, processing of the level 1A data to level 2 was made again but this time with the inclusion of calculations for water-leaving reflectances at 765 and 865 nm according to the new turbid water algorithm and subtraction of these reflectances from the Rayleigh-corrected reflectances. The resultant imagery is shown in Figs. 5 and 6 for 443 and 670 nm, respectively. The improvement over Figs. 2 and 3 is clear. With the turbid water atmospheric correction, physically realistic (positive) values are obtained for water-leaving radiances at all cloud-free pixels for 443 and at 670 nm. Moreover, the spatial structures observed in Fig. 6 correlate well with known SPM distributions. At 412 nm (not shown), whereas turbid coastal waters now show positive water-leaving radiance as well as realistic spatial structures, areas of negative water-leaving radiance persist for deeper water. This result might be attributed to an overestimated $\varepsilon_m^{(7,8)}$, but further tests show that results are not strongly sensitive to small (e.g., 0.05) variations in $\varepsilon_m^{(7,8)}$. Because of the weakness of the water-leaving signal compared with the atmospheric signal at 412
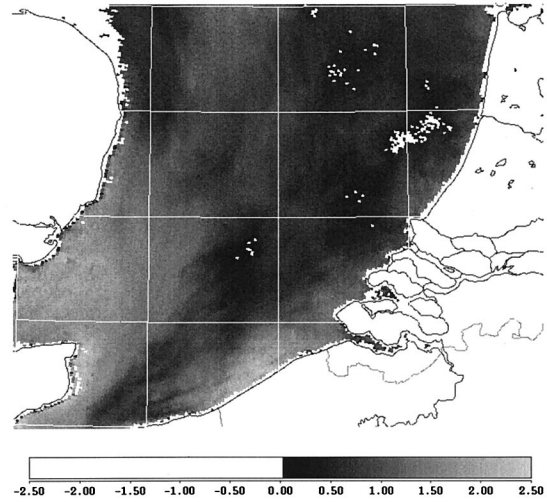
nm, it is likely then that other components of the processing chain may also require refinement if reliable 412-nm water-leaving radiances are to be achieved. A full system error analysis is beyond the scope of the present study, although elements that warrant analysis include calculation of Rayleigh reflectance, absolute sensor calibration, whitecap correction, and the tabulated aerosol models.

Normalized water-leaving radiance spectra are shown in Fig. 7 for sample turbid water and clearer water pixels. The effect of the new algorithm on raising radiance values throughout the spectrum and particularly at shorter wavelengths is clearly seen. For the turbid water pixel the 412-nm radiance has become positive. For the clearer water pixel, although the 412-nm radiance is still negative, with the new algorithm its absolute value is now very small and could be highly sensitive to other components of
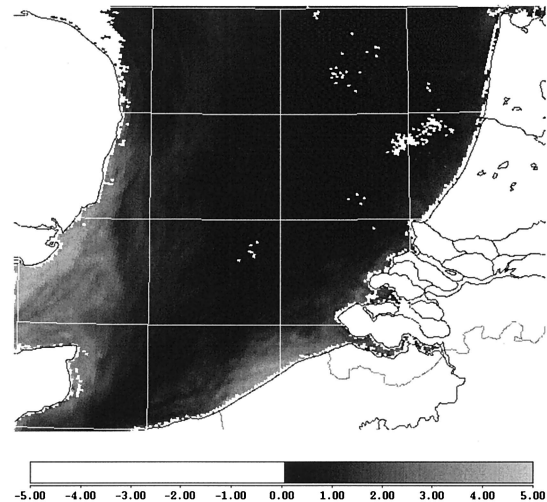

Fig. 6. Normalized water-leaving radiance (mW cm^{-2} μm^{-1} sr^{-1}) for the SeaWiFS image taken 28 October 1997, 12:15 UTC, at 670 nm after the turbid water atmospheric correction.
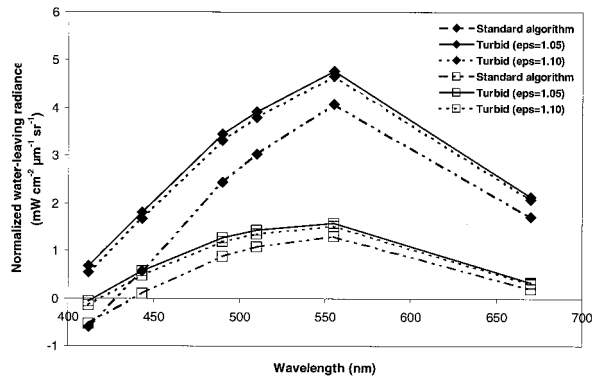
Fig. 7. Normalized water-leaving radiances for a typical turbid water point (filled diamonds) and a clearer offshore pixel (open squares) obtained with the standard atmospheric correction (dashed–dotted curves) and with the new turbid water atmospheric correction with eps $= \varepsilon_m^{(7,8)} = 1.05$ (solid curves) and eps $= \varepsilon_m^{(7,8)} = 1.10$ (dashed curves).
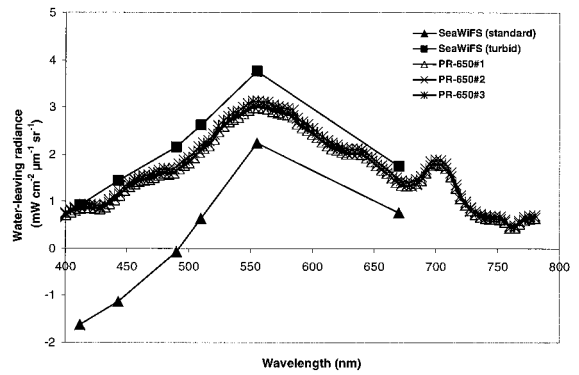

Fig. 8. Comparison of *in situ* PR-650 colorimeter measurements of water-leaving radiance for Lake Markermeer taken on 25 June 1999 at 12:48 UTC with coincident spectra from the SeaWiFS image acquired at 11:31 UTC and processed with the standard and the new turbid water atmospheric correction algorithms.

the processing chain such as calculation of Rayleigh reflectances.

This procedure has now been applied to a total of ten SeaWiFS images of this region with similar success. In all cases physically realistic imagery has been achieved for nearly all cloud-free pixels at 443 nm and for most pixels at 412 nm. Inspection of the scatterplots gave no reason to suppose a temporal variation of α, which was set equal to 1.72 for all images, although an uncertainty of ~0.1 is estimated for good images (uncontaminated by clouds or contrails). Some image-to-image variation of $\varepsilon_m^{(7,8)}$ was necessary in view of the slightly different slopes found in the scatterplots. For the SeaWiFS images considered, which spanned a whole year, $\varepsilon_m^{(7,8)}$ was set to a value between 1.00 and 1.12 with an estimated uncertainty of 0.05 for each image.

B. Comparison with Measurements for Lake Markermeer

A first validation of the method with *in situ* measurements was performed for Lake Markermeer, a large, shallow, and highly turbid Dutch inland body of water located at (52°30′N, 5°20′E) with an area of 610 km^2, a mean depth of 3 m, and Secchi depths from 0.2 to 0.6 m. Above-water radiance spectra were collected for this lake on 25 June 1999 with a PR-650 SpectraColorimeter (manufactured by Photo Research). This equipment was used previously for chlorophyll detection in such waters,[44] and its characteristics and use are described in more detail in Ref. 44. The PR-650 colorimeter has 1° measuring optics and a 128-element diode array, acquiring spectra from 380 to 780 nm with a full bandwidth at half-maximum of 8 nm. The instrument was hand held by an operator aboard the research vessel Markermeer approximately 4 m above the water surface and pointed at the water in a plane at right angles to the vertical plane of the Sun and for a nadir angle of observation of 42°. The target water surface has a diameter of approximately 0.1–0.2 m. To assess temporal fluctuations arising from surface waves and

illumination conditions we made three spectral scans consecutively with a sampling time of 1600 ms for each scan.

One such triplet observation was made at 12:48 UTC at (52°28.4′N, 5°18.3′E) and is close in time to a cloud-free SeaWiFS image acquired at 11:31 UTC. Weather conditions at the time of this observation were good (1/8 cloud coverage; wind speed, 5 m/s with some Langmuir streaks visible; wave height, 0.2 m). Measurements of water samples indicate high chlorophyll concentration (64 μg/L), corresponding to blue-green algae observed in the water column (not floating), and a high total concentration (41 mg/L) of SPM and a Secchi depth of 0.2 m were recorded.

For the corresponding SeaWiFS image, atmospheric conditions seem good (no obvious haze or clouds for the region of measurements), although some difficulties may be expected because of the high sensor zenith angle (53°) and the possibility of stray light or adjacency effects because of proximity to land. After inspection of the Rayleigh-corrected band 7:8 reflectance scatterplot this image was processed with $\varepsilon_m^{(7,8)} = 1.05$ and $\alpha = 1.72$, with the error flag[42] for high (above-knee) radiance disabled. The SeaDAS software was modified to give above-water radiances, including whitecap radiance.

A comparison of SeaWiFS-derived above-water radiance, corrected to correspond to the solar zenith angle at the moment of the *in situ* measurements, against the PR-650 colorimeter measurements is shown in Fig. 8 for both the standard atmospheric correction and the new turbid water algorithm. Although there is a noticeable offset between the data from the turbid water algorithm and the *in situ* measurements, the spectral form is well produced by the turbid water algorithm. This comparison results from a first application of the algorithm, and no attempt has been made to tune results to give better agreement between image data and measurements because differences may arise from many factors including spatial averaging of image data (a difference

in spatially averaged backscatter coefficient could easily produce a multiplicative offset similar to that seen in Fig. 8), different viewing angles, temporal variability of illumination conditions, proximity of pixel to land, and various components of the SeaWiFS processing chain as well as the turbid water atmospheric correction itself. In any case it is clear that the new algorithm is far superior to the standard algorithm, which gives negative water-leaving radiances for 412–490 nm in this case (and assumes zero water-leaving radiance at 765 nm) and suggests an error, increasing toward lower wavelengths, that is typical of excessive aerosol path radiance removal.

4. Conclusions

An algorithm to perform atmospheric correction of SeaWiFS data for turbid coastal waters has been described and tested. This algorithm replaces the assumptions of the standard SeaWiFS atmospheric correction algorithm of zero water-leaving radiance at the two near-infrared bands by the assumptions of spatial homogeneity of the 765:865-nm ratio of the aerosol reflectance $\varepsilon_m^{(7,8)}$ and of the water-leaving reflectance α. The former assumption represents a reversion to methods used previously with the CZCS and as such may suffer from similar inaccuracies when aerosol type varies within a scene: In effect the extra information available in SeaWiFS, which is used in the standard algorithm to permit a pixel-by-pixel variation of aerosol type, is used in the present algorithm to permit instead calculation of nonzero near-infrared water-leaving radiances. The latter assumption can be expected to be rather more valid than similar relations developed for CZCS bands because in the near infrared optical properties are dominated by particulate backscatter and pure water absorption alone. Calibration of $\varepsilon_m^{(7,8)}$ is determined on an image-by-image basis from inspection of the scatterplot of the Rayleigh-corrected reflectances for these two bands. A rather general calibration of α was made from theoretical considerations of near-infrared optical properties. Implementation of the turbid water extended atmospheric correction is achieved by a two-pass procedure within the SeaDAS software. In the first pass, Rayleigh-corrected reflectances for the near-infrared bands are calculated and output in the form of a scatterplot for subjective estimation of $\varepsilon_m^{(7,8)}$. In the second pass this parameter is used to perform the atmospheric correction. Because of this two-pass procedure associated with $\varepsilon_m^{(7,8)}$ calibration, this algorithm is better suited to regional studies in which each image is individually treated rather than for fully automatic global processing.

The application of the method to a SeaWiFS image of the Belgian coastal waters was demonstrated. In the standard algorithm (designed for clear open ocean waters) the aerosol reflectance ratio is severely overestimated, giving unphysical negative water-leaving radiances at 412 and 443 nm, complete failure of the atmospheric correction, or both. Because regions of known turbid water can be identified in the top-of-atmosphere radiances for the near-infrared

bands, this failure can clearly be attributed to the invalidity of the assumption of zero water-leaving radiance for these bands. In the turbid water extension of the standard algorithm such problems are overcome and water-leaving radiances are positive for all cloud-free pixels at bands from 443 to 670 nm and for turbid coastal pixels at 412 nm. A further qualitative indication of performance is given by the derived 865-nm aerosol reflectance map (not shown), which no longer shows spatial structures known to be related in reality to regions of turbid water.

A preliminary validation of the algorithm was made by comparison of SeaWiFS-derived water-leaving radiance spectra with *in situ* measurements for Lake Markermeer in The Netherlands. Notwithstanding the well-known difficulties involved in comparing image data with *in situ* data (slight asynchronicity, different areas for spatial averaging, etc.) as well as the possibility that many other aspects of SeaWiFS image processing may correspond to observed differences, the results are encouraging: Whereas the standard atmospheric correction algorithm shows a clear underestimation of water-leaving radiances with increasing error toward lower wavelengths (typical of excessive aerosol path radiance removal), the turbid water extended algorithm gives good reproduction of the water-leaving radiance spectral form.

A detailed theoretical analysis has been made of the sensitivity of results to the choice of the two calibration parameters. Typical errors in estimating $\varepsilon_m^{(7,8)}$ and α of $\Delta\varepsilon_m^{(7,8)} = \pm 0.05$ and $\Delta\alpha = \pm 0.22$, respectively, give corresponding water-leaving reflectance errors of the order of $\Delta\rho_w^{(i)} = \pm 0.01$ for turbid water with a turbid atmosphere or a proportionally smaller error according to Eq. (A8) below for clearer atmospheric and marine conditions. The causes of possible spatial and temporal variability of $\varepsilon_m^{(7,8)}$ and α have been discussed. In the case of estimation of α the largest uncertainty concerns the poorly known spectral variation of particulate backscatter. Few *in situ* measurements have been reported of particulate backscatter or reflectance in the range 700–900 nm, although there are notable exceptions.[32,45,46] We note that the use of a third red or near-infrared band may further reduce the errors associated with calibration of α.

The present algorithm is similar in many ways to the approach of Arnone *et al*.[23] Both algorithms recognize the need to remove near-infrared water-leaving reflectance from the 765- and 865-nm bands before calculation of aerosol path reflectance and exploit the simple nature of inherent optical properties in the near-infrared range to provide relations between these water-leaving reflectances. The essential difference lies in the number of bands used. The inclusion of a third band at 670 nm in the algorithm of Arnone *et al*. replaces the assumption of spatial homogeneity of the aerosol path reflectance ratio, allowing a pixel-by-pixel approach to be retained with consequent advantages for automation of the procedure and treatment of scenes with variable aerosol types. However, that approach assumes that the influence of chlorophyll absorption on reflectance at

670 nm is negligible, which may not always be the case. The disadvantages of both algorithms clearly arise from the limited number of near-infrared bands available with SeaWiFS—for future sensors the use of extra bands will allow the assumptions used in both algorithms to be relaxed, providing greater accuracy and generality.

Although they have been described in the context of SeaWiFS imagery, the basic assumptions of the turbid water algorithm can be applied rather generally to other satellite-based and probably also airborne ocean color sensors. In view of the large number of such sensors in operation or planned for the coming years as well as the popularity of airborne systems, it is useful to consider the extension of this algorithm to different wavelength combinations. Whereas SeaWiFS represents a huge improvement over the CZCS for atmospheric correction purposes because of the two near-infrared bands, further information, particularly regarding the wavelength dependence of the hydrosol backscattering coefficient, would reduce further the errors involved in atmospheric correction over turbid waters. This information could be sought in available visible bands by an appropriate ocean color model; however, the additional complication of absorption by CDOM and phytoplankton and its degradation products significantly complicates the task. Further information could also be derived from local knowledge of inherent optical properties, especially the backscatter coefficient spectral form, based on *in situ* measurement campaigns.[39,47–49] However, the addition of at least one more red or near-infrared band would permit a further degree of freedom, such as backscatter coefficient wavelength-dependency exponent n, to be modeled, thus (it is hoped) reducing the atmospheric correction error, particularly for the blue and near-ultraviolet bands. For example, the parameter $\varepsilon_m^{(7,8)}$, calibrated here by inspection of Rayleigh-corrected scatterplots, could be deduced on a pixel-by-pixel basis by satellite data alone, and the assumption of spatial homogeneity of this parameter could be relaxed. In this respect the far superior spectral coverage planned for the MERIS and the Moderate Resolution Imaging Spectrometer (MODIS) is promising, and such a turbid water atmospheric correction algorithm is already envisaged[24] for generation of the standard MERIS case 2 water products. For AVHRR the nonzero water-leaving radiance for near-infrared band 2 has been mentioned or modeled by a number of authors.[50–52] Despite the limited spectral information provided by the two AVHRR bands, the present algorithm could still be applied, in which case the two water-leaving reflectances from Eqs. (25) and (27) would be used directly as the end products.

In the context of chlorophyll retrieval in turbid coastal and inland waters an atmospheric correction algorithm based on near-infrared bands is highly complementary to an ocean color model based on red bands and exploiting the chlorophyll absorption peak near 670 nm, the chlorophyll fluorescence at 683 nm, or both.[53–55] For wavelengths from 600 to 1000 nm the absorption by CDOM and detritus is low and spectrally rather flat. Moreover, the errors involved in extrapolating aerosol reflectance to red bands are considerably smaller than for wavelengths less than 450 nm.

The directions for further research on turbid water atmospheric correction include a more detailed analysis of *in situ* inherent optical properties and reflectance measurements for the range 700–900 nm; wider application of the algorithm to offshore, coastal, and inland waters; application of the technique in a multisensor perspective; and coupling of the technique with a bio-optical model for SPM and chlorophyll retrieval.[3]

Appendix A: Derivation of Error Estimates

In this appendix an estimate for the errors associated with the assumptions inherent in this turbid water atmospheric correction is derived. For this estimate the following simplifications are made:

The spectral form of the aerosol reflectance ratio can be approximated by[13]

$$\varepsilon_m^{(i,8)} = \exp[c(\lambda_8 - \lambda_i)] \tag{A1}$$

for a suitable (local) choice of c. Eliminating c by expressing $\varepsilon_m^{(i,8)}$ in terms of $\varepsilon_m^{(7,8)}$ gives

$$\varepsilon_m^{(i,8)} = [\varepsilon_m^{(7,8)}]^{\delta_i}, \tag{A2}$$

where

$$\delta_i = \frac{\lambda_8 - \lambda_i}{\lambda_8 - \lambda_7}. \tag{A3}$$

Single- and multiple-scattering aerosol reflectance ratios are assumed equal:

$$\frac{\rho_{\mathrm{am}}^{(i)}}{\rho_{\mathrm{am}}^{(8)}} = \varepsilon_{s(I)}^{(i,8)}, \tag{A4}$$

with

$$\varepsilon_m^{(i,8)} = \varepsilon_{s(I)}^{(i,8)} \tag{A5}$$

and, thus, the combination of Eqs. (A4), (A5), and (A2) yields

$$\rho_{\mathrm{am}}^{(i)} = [\varepsilon_m^{(7,8)}]^{\delta_i}\rho_{\mathrm{am}}^{(8)}. \tag{A6}$$

The atmospheric transmittance factor $t_{v*}^{(i)}$ is assumed to be approximately independent of aerosol properties

Then, when we denote the errors (that arise from spatial variability or other factors) in estimation of the calibration parameters $\varepsilon_m^{(7,8)}$ and α by $\Delta\varepsilon_m^{(7,8)}$ and $\Delta\alpha$, respectively, and the consequent error in water-leaving reflectance at band i by $\Delta\rho_w^{(i)}$, differentiation of Eq. (16) gives

$$\Delta\rho_w^{(i)} = -\frac{1}{t_{v*}^{(i)}}\left[\frac{\partial\rho_{\mathrm{am}}^{(i)}}{\partial\varepsilon_m^{(7,8)}}\Delta\varepsilon_m^{(7,8)} + \frac{\partial\rho_{\mathrm{am}}^{(i)}}{\partial\alpha}\Delta\alpha\right], \tag{A7}$$

which, after Eqs. (A6) and (24) are used to express $\rho_{am}^{(i)}$ as a function of $\varepsilon_m^{(7,8)}$ and α and after the partial differentiation, yield

$$\Delta\rho_w^{(i)} = -\frac{1}{t_{v*}^{(i)}}\varepsilon_m^{(i,8)}\left[K^{(i)}\rho_{am}^{(8)}\Delta\varepsilon_m^{(7,8)} + \frac{t_{v*}^{(8)}}{\alpha - \varepsilon_m^{(7,8)}}\rho_w^{(8)}\Delta\alpha\right],$$

(A8)

where

$$K^{(i)} = \frac{\delta_i}{\varepsilon_m^{(7,8)}} + \frac{1}{\alpha - \varepsilon_m^{(7,8)}}.$$

(A9)

In Eq. (A8) the first term, which is proportional to the aerosol path radiance, will be important for clear water regions, whereas the second term, which is proportional to the water-leaving radiance, will dominate in turbid water regions.

Appendix B: Sensitivity to Calibration of Water-Leaving Reflectance Ratio

In this appendix, to estimate the errors introduced by the assumption of a spatially homogeneous ratio for the water-leaving reflectance, we assess the uncertainty in calibration of α by examining each of the assumptions that underlie Eqs. (28)–(31). Remaining consistent with a first-order estimate of this uncertainty, we address each assumption in turn, using a more comprehensive or higher-order model, and calculate the corresponding perturbation to α with respect to the first estimate, which is defined as

$$\alpha_0 = \frac{a_w^{(8)}}{a_w^{(7)}}.$$

(B1)

1. Internal Reflection of the Upwelling Radiance Field by the Sea Surface

Replacing Eq. (28) by a more comprehensive marine reflectance model,[26] including internal reflection of the upwelling radiance field by the sea surface, gives

$$\frac{R}{1 - rR} = \frac{1}{M}\frac{Q}{\pi}\frac{\rho_w}{T_0},$$

(B2)

where $r \approx 0.48$ is the water–air reflectance for totally diffuse irradiance. This leads to

$$\alpha = \frac{R_7}{R_8}\frac{1 - rR_8}{1 - rR_7}.$$

(B3)

From Eqs. (29)–(31), $R_7 = \alpha_0 R_8$ and, to first order in R_8,

$$\alpha = \alpha_0(1 - rR_8[1 - \alpha_0]).$$

(B4)

For an unfavorable case of highly turbid water, $R_8 = 0.02$ gives

$$\alpha = \alpha_0(1 + 0.48 \times 0.02 \times 0.72) = 1.007\alpha_0.$$ (B5)

2. Second-Order Scattering in Reflectance–Inherent-Optical-Property Model

If the second-order terms in $(b_b/a)^2$ found from a Taylor expansion of the marine reflectance model[26] are included in Eq. (29), then the subsurface irradiance reflectance is related to the inherent optical properties by

$$\frac{R}{Q} = l_1\frac{b_b}{a} + l_2^*\left(\frac{b_b}{a}\right)^2,$$

(B6)

where $l_2^* = 0.0794 - 0.0949$. From Eqs. (28), (30), and (31), this gives

$$\alpha = \frac{\rho_w^{(7)}/T_0^{(7)}}{\rho_w^{(8)}/T_0^{(8)}} = \left\{l_1\frac{b_b}{a_w^{(7)}} + l_2^*\left[\frac{b_b}{a_w^{(7)}}\right]^2\right\}$$
$$\times \left\{l_1\frac{b_b}{a_w^{(8)}} + l_2^*\left[\frac{b_b}{a_w^{(8)}}\right]^2\right\}^{-1}$$
$$= \frac{a_w^{(8)}}{a_w^{(7)}}\left\{1 + \frac{l_2^*}{l_1}\left[\frac{b_b}{a_w^{(7)}}\right]\right\}\left\{1 + \frac{l_2^*}{l_1}\left[\frac{b_b}{a_w^{(8)}}\right]\right\}^{-1},$$

(B7)

which gives to second order in (b_b/a)

$$\alpha = \alpha_0\left\{1 + \frac{l_2^*}{l_1}\left[\frac{b_b}{a_w^{(7)}} - \frac{b_b}{a_w^{(8)}}\right]\right\}.$$

(B8)

Rewriting the first-order term as a function of subsurface irradiance reflectances and using $R_7 = \alpha_0 R_8$ give, when we drop second-order reflectance terms,

$$\alpha = \alpha_0\left[1 + \frac{l_2^*}{Ql_1^2}(R_7 - R_8)\right] = \alpha_0\left[1 + \frac{l_2^*}{Ql_1^2}R_8(\alpha_0 - 1)\right],$$

(B9)

and evaluating this expression for $R_8 = 0.02$ and assuming that $Q = \pi$ give

$$\alpha = 0.992\alpha_0.$$

(B10)

3. Absorption from Other Water Constituents

We can evaluate the approximation [Eq. (30)] that the only absorbing substance is pure water itself by setting upper limits for absorption from other water constituents. Small changes, $a_*^{(7)}$ and $a_*^{(8)}$, in the total absorption coefficient can arise from additional absorption by constituents such as phytoplankton, detritus, or CDOM; i.e.,

$$a(\lambda_7) = a_w^{(7)} + a_*^{(7)},$$

(B11)

$$a(\lambda_8) = a_w^{(8)} + a_*^{(8)}.$$

(B12)

It is then easy to show that, to first order in these perturbations,

$$\alpha = \alpha_0\left[1 + \frac{a_*^{(8)}}{a_w^{(8)}} - \frac{a_*^{(7)}}{a_w^{(7)}}\right].$$

(B13)

Little published information is available on inherent optical properties in the near-infrared spectral

range because of great difficulties in measurement of such small absorption values compared with the large absorption of pure water, which is itself not well known. However, in one data set[56] nonwater absorption coefficients are reported for a near-shore station of ~ 0.01 m^{-1} at 750 nm. Taking such a value for $a_*^{(7)}$ and assuming the unfavorable case that such nonwater absorption is not spectrally flat but has $a_*^{(8)} = 0$ give

$$\alpha = \alpha_0\left(1 - \frac{0.01\text{ m}^{-1}}{2.59\text{ m}^{-1}}\right) = 0.996\alpha_0. \qquad \text{(B14)}$$

Possible variations in the absorption of pure water caused, for example, by variations in temperature or other environmental parameters are not well understood. However, for the example[57] of a 2% variation in pure water absorption at 750 nm for a temperature variation of 5 °C, the effect of similar spatial variations in temperature would give a corresponding 2% variation in α.

4. Spectral Variation of Particulate Backscatter

Models for the spectral variation of particulate backscatter generally take the form

$$b_b(\lambda) = b_{b0}(\lambda/\lambda_0)^{-n}, \qquad \text{(B15)}$$

where b_{b0} is the backscatter coefficient at reference wavelength λ_0 and n is a parameter related to particle size distribution.[1,31,47,58,59] In the estimation of α_0 the value of $n = 0$ was used. For nonzero n, Eqs. (28)–(30) give

$$\alpha = \alpha_0\left(\frac{\lambda_7}{\lambda_8}\right)^{-n} = \alpha_0\left(\frac{765\text{ nm}}{865\text{ nm}}\right)^{-n}, \qquad \text{(B16)}$$

and $n = 1$ and $n = 2$ give $\alpha = 1.13\alpha_0$ and $\alpha = 1.28\alpha_0$, respectively. Thus uncertainty in the spectral variation of particulate backscatter is seen to have some influence on the calibration of α.

5. Sensor Response Function

In Eq. (33) a delta function sensor response function was assumed with central wavelengths of 765 and 865 nm. It is beyond the scope of the present study to consider how the actual sensor response function[60] would affect results. However, a simple estimate can easily be made of the sensitivity of calibration of α to one aspect of the sensor response function, the central wavelength. Thus, assuming actual central wavelengths of 764.9 and 866.4 nm and using the data of Palmer and Williams[36] give

$$\alpha = \frac{a_w(866.4\text{ nm})}{a_w(764.9\text{ nm})} = 1.74. \qquad \text{(B17)}$$

6. Summary of Calibration Sensitivity of Water-Leaving Reflectance Ratio

A comparison of the second-order effects considered in this appendix shows that by far the most important relates to possible wavelength dependence of particulate backscatter, suggesting that investigation of this dependent backscatter should be a high priority for any further refinement of this algorithm. *In situ* measurement of particulate backscatter spectra (or reflectance spectra) in the range 700–900 nm could provide information for a region-specific calibration of n and hence of α to reduce this error. However, for future sensors such as the MERIS the use of an extra near-infrared band to deduce α is probably preferable, as for coastal waters n may be highly variable in time and space because of the influence of resuspension processes on suspended particle size distributions.

Appendix C. Symbols Used in This Paper

a Absorption coefficient (total),

a_w pure water absorption coefficient,

b_b backscatter coefficient,

b_{b0} backscatter coefficient at reference wavelength,

f^I function relating single- to multiple-scattering aerosol reflectance for model I,

F_0 extraterrestrial solar irradiance,

g^I function relating multiple- to single-scattering aerosol reflectance for model I,

$K^{(i)}$ factor used in error analysis, defined in Eq. (A9),

l_1, l_2^* marine reflectance model constants,

L upward radiance,

L_w water-leaving radiance,

$[L_w]_N$ normalized water-leaving radiance,

M constant relating above- and below-surface irradiance ratios,

n backscatter coefficient spectral exponent,

Q factor relating upwelling radiance to upwelling irradiance,

R subsurface irradiance reflectance,

$t_{0(x)}$ sun–sea transmittance factor for process x,

$t_{v(x)}$ sea–sensor transmittance factor for process x,

t_{v*} atmospheric transmittance factor, defined by Eq. (9),

T_0 atmospheric transmittance sun–sea,

T_v atmospheric transmittance sea-sensor,

α imposed water reflectance ratio for bands 7:8,

α_0 first-order estimate of water reflectance ratio for bands 7:8,

δ_i wavelength extrapolation factor, defined by Eq. (A3),

$\Delta\alpha$ error in calibration constant α,

$\Delta\varepsilon_m^{(7,8)}$ error in calibration constant $\varepsilon_m^{(7,8)}$,

$\Delta\rho_w^{(i)}$ error in water reflectance at SeaWiFS band i,

$\varepsilon_m^{(7,8)}$ imposed multiple-scattering aerosol reflectance ratio, bands 7:8,

$\varepsilon_{s(I)}^{(i,j)}$ theoretical single-scattering aerosol reflectance ratio, bands i:j, aerosol model I,

$\varepsilon_{*s(I)}^{(i,j)}$ retrieved single-scattering aerosol reflectance ratio, bands i:j, aerosol model I,

λ wavelength,

λ_i wavelength at SeaWiFS band i,

θ_0 solar zenith angle,

ρ reflectance using normalization [Eq. (1)],

$\rho_a^{(i)}$ aerosol reflectance at SeaWiFS band i,

$\rho_{am}^{(i)}$ multiple-scattering aerosol plus Rayleigh-aerosol reflectance at SeaWiFS band i,

$\rho_{ar}^{(i)}$ Rayleigh-aerosol interaction reflectance at SeaWiFS band i,

$\rho_{as(I)}^{(i)}$ single-scattering aerosol reflectance at SeaWiFS band i, aerosol model I,

$\rho_c^{(i)}$ Rayleigh-corrected reflectance at SeaWiFS band i,

$\rho_r^{(i)}$ Rayleigh reflectance at SeaWiFS band i,

$\rho_t^{(i)}$ total top-of-atmosphere reflectance at SeaWiFS band i,

$\rho_w^{(i)}$ water reflectance at SeaWiFS band i,

$\rho_{wc}^{(i)}$ whitecap reflectance at SeaWiFS band i.

References

1. A. Morel and L. Prieur, "Analysis of variations in ocean color," Limnol. Oceanogr. **22,** 709–722 (1977).

2. S. Sugihara, M. Kishino, and N. Okami, "Estimation of water quality parameters from irradiance reflectance using optical models," J. Oceanogr. Soc. Jpn **41,** 399–406 (1985).

3. A. P. Vasilkov, "A retrieval of coastal water constituent concentrations by least-square inversion of a radiance model," in *4th International Conference on Remote Sensing for Marine and Coastal Environments* (Environmental Research Institute of Michigan Ann Arbor, Mich., 1997), Vol. II, pp. 107–116.

4. Z. Lee, K. L. Carder, S. K. Hawes, R. G. Steward, T. G. Peacock, and C. O. Davis, "Model for the interpretation of hyperspectral remote-sensing reflectance," Appl. Opt. **33,** 5721–5732 (1994).

5. S. Tassan, "Local algorithms using SeaWiFS data for the retrieval of phytoplankton, pigments, suspended sediment, and yellow substance in coastal waters," Appl. Opt. **33,** 2369–2378 (1994).

6. A. G. Dekker, H. J. Hoogenboom, L. M. Goddijn, and T. J. M. Malthus, "The relation between inherent optical properties and reflectance spectra in turbid inland waters," Remote Sens. Rev. **15,** 59–74 (1997).

7. S. Sathyendranath, L. Prieur, and A. Morel, "An evaluation of the problems of chlorophyll retrieval from ocean colour, for case 2 waters," Adv. Space Res. **7,** 27–30 (1987).

8. R. Doerffer and J. Fischer, "Concentrations of chlorophyll, suspended matter, *gelbstoff* in case II waters derived from satellite coastal zone color scanner data with inverse modeling methods," J. Geophys. Res. **99,** 7457–7466 (1994).

9. M. Viollier, D. Tanré, and P. Y. Deschamps, "An algorithm for remote sensing of water color from space," Boundary-Layer Meteorol. **18,** 247–267 (1980).

10. B. Sturm, "The atmospheric correction of remotely sensed data and the quantitative determination of suspended matter in marine water surface layers," in *Remote Sensing in Meteorology, Oceanography and Hydrology*, A. P. Cracknell, ed. (Ellis Horwood, Chichester, UK, 1980), pp. 163–197.

11. H. R. Gordon, "Removal of atmospheric effects from satellite imagery of the oceans," Appl. Opt. **17,** 1631–1636 (1978).

12. H. R. Gordon and D. J. Castano, "Coastal Zone Color Scanner atmospheric correction algorithm: multiple scattering effects," Appl. Opt. **26,** 2111–2122 (1987).

13. H. R. Gordon and M. Wang, "Retrieval of water-leaving radiance and aerosol optical thickness over the oceans with SeaWiFS: a preliminary algorithm," Appl. Opt. **33,** 443–452 (1994).

14. M. Viollier and B. Sturm, "CZCS data analysis in turbid coastal waters," J. Geophys. Res. **89,** 4977–4985 (1984).

15. R. C. Smith and W. H. Wilson, "Ship and satellite bio-optical research in the California Bight," in *Oceanography from Space*, J. F. R. Gower, ed. (Plenum, New York, 1981), pp. 281–294.

16. R. W. Austin and T. J. Petzold, "The determination of the diffuse attenuation coefficient of sea water using the Coastal Zone Color Scanner (CZCS)," in *Oceanography from Space*, J. F. R. Gower, ed. (Plenum, New York, 1981), pp. 239–255.

17. J. L. Mueller, "Effects of water reflectance at 670 nm on Coastal Zone Color Scanner (CZCS) aerosol radiance estimates off the coast of central California," in *Ocean Optics VII*, M. A. Blizard, ed., Proc. SPIE **489,** 179–186 (1984).

18. R. W. Gould and R. A. Arnone, "Extending Coastal Zone Color Scanner estimates of the diffuse attenuation coefficient into Case II waters," in *Ocean Optics XII*, J. S. Jaffe, ed., Proc. SPIE **2258,** 342–356 (1994).

19. T. Aarup, S. Groom, and P. M. Holligan, "The processing and interpretation of North Sea CZCS imagery," Neth. J. Sea Res. **25,** 3–9 (1990).

20. A. Bricaud and A. Morel, "Atmospheric corrections and interpretation of marine radiances in CZCS imagery: use of a reflectance model," Oceanol. Acta **7,** 33–50 (1987).

21. F. M. Guan, J. Pelaez, and R. H. Stewart, "The atmospheric correction and measurement of chlorophyll concentration using the Coastal Zone Color Scanner," Limnol. Oceanogr. **30,** 273–285 (1985).

22. P. E. Land and J. D. Haigh, "Atmospheric correction over case 2 waters with an iterative fitting algorithm," Appl. Opt. **35,** 5443–5451 (1996).

23. R. A. Arnone, P. Martinolich, R. W. Gould, R. Stumpf, and S. Ladner, "Coastal optical properties using SeaWiFS," presented at Ocean Optics XIV Conference, Kailua-Kona, Hawaii, 10–13 November 1998. Ocean Optics XIV CD-ROM (Office of Naval Research, Washington, D.C., 1998).

24. J. Aiken and G. Moore, "MERIS algorithm theoretical basis document: case 2 (S) bright pixel atmospheric correction," Rep. PO-TN-MEL-GS-0005 (Plymouth Marine Laboratory, Plymouth, UK, 1997).

25. H. R. Gordon and D. K. Clark, "Clear water radiances for atmospheric correction of coastal zone color scanner imagery," Appl. Opt. **20,** 4175–4180 (1981).

26. H. R. Gordon, O. B. Brown, R. H. Evans, J. W. Brown, R. C. Smith, K. S. Baker, and D. K. Clark, "A semianalytical radiance model of ocean color," J. Geophys. Res. **93,** 10,909–10,924 (1988).

27. H. R. Gordon and M. Wang, "Influence of oceanic whitecaps on atmospheric correction of ocean-color sensors," Appl. Opt. **33,** 7754–7763 (1994).

28. M. Wang, "Atmospheric correction of ocean color sensors:

computing atmospheric diffuse transmittance," Appl. Opt. **38,** 451–455 (1999).

29. H. Yang and H. R. Gordon, "Remote sensing of ocean color: assessment of water-leaving radiance bidirectional effects on atmospheric diffuse transmittance," Appl. Opt. **36,** 7887–7897 (1997).

30. K. Ding and H. R. Gordon, "Analysis of the influence of O2 A band absorption on atmospheric correction of ocean color imagery," Appl. Opt. **34,** 8363–8374 (1995).

31. C. H. Whitlock, L. R. Poole, J. W. Usry, W. M. Houghton, W. G. Witte, W. D. Morris, and E. A. Gurganis, "Comparison of reflectance with backscatter and absorption parameters for turbid waters," Appl. Opt. **20,** 1696–1703 (1981).

32. S. Ouillon, P. Forget, J. M. Froidefond, and J. J. Naudin, "Estimating suspended matter concentrations from SPOT data and from field measurements in the Rhone River plume," Mar. Technol. Soc. J. **31,** 15–20 (1997).

33. G. J. Prangsma and J. N. Roozekrans, "Using NOAA AVHRR imagery in assessing water quality parameters," Int. J. Remote Sens. **10,** 811–818 (1989).

34. J. M. Andre and A. Morel, "Atmospheric corrections and interpretation of marine radiances in CZCS imagery, revisited," Oceanol. Acta **14,** 3–22 (1991).

35. R. W. Preisendorfer, "Application of radiative transfer theory to light measurements in the sea," Monograph Rep. 10 (International Union for Geodesy and Geophysics, Paris, 1961).

36. K. F. Palmer and D. J. Williams, "Optical properties of water in the near infrared," J. Opt. Soc. Am. **64,** 1107–1110 (1974).

37. G. Fu, K. S. Baith, and C. R. McClain, "SeaDAS: The SeaWiFS data analysis system," presented at the 4th Pacific Ocean Remote Sensing Conference, Qingdao, China, 28–31 July 1998.

38. C. F. Jago, A. J. Bale, M. O. Green, M. J. Howarth, S. E. Jones, I. N. McCave, G. E. Millward, A. W. Morris, A. A. Rowden, and J. J. Williams, "Resuspension processes and seston dynamics, southern North Sea," in *Understanding the North Sea System*, H. Charnock, K. R. Dyer, J. M. Huthnance, P. S. Liss, J. H. Simpson, and P. B. Tett, eds. (Chapman & Hall, London, 1994), pp. 97–113.

39. I. J. A. Althuis, J. Vogelzang, M. R. Wernand, S. J. Shimwell, W. W. C. Gieskes, R. E. Warnock, J. Kromkamp, R. Wouts, and W. Zevenboom, "On the colour of case II waters: Particulate matter North Sea," Rep. 95-21B (Beleidscommissie Remote Sensing, Delft, The Netherlands, 1996).

40. C. Lancelot, V. Rousseau, G. Billen, and D. V. Eeckhout, "Coastal eutrophication of the Southern Bight of the North Sea: assessment and modelling," in *Sensitivity to Change: Black Sea, Baltic Sea and North Sea*, E. Ozsoy and A. Mikaelyan, eds. (Kluwer Scientific, Dordrecht, The Netherlands, 1997), pp. 437–454.

41. C. R. McClain, M. L. Cleave, G. C. Feldman, W. W. Gregg, S. B. Hooker, and N. Kuring, "Science quality SeaWiFS data for global biosphere research," Sea Technol. **9,** 10–16 (1998).

42. C. R. McClain, K. Arrigo, W. E. Esaias, M. Darzi, F. S. Patt, R. H. Evans, J. W. Brown, C. W. Brown, R. A. Barnes, and L. Kumar, "SeaWiFS algorithms, Part 1," SeaWiFS Tech. Rep. 28, NASA Tech. Memo. 104566 (NASA, Greenbelt, Md., 1995).

43. B. A. Eckstein and J. J. Simpson, "Cloud screening Coastal Zone Color Scanner images using channel 5," Int. J. Remote Sens. **12,** 2359–2377 (1991).

44. H. J. Gons, "Optical teledetection of chlorophyll a in turbid inland waters," Environ. Sci. Technol. **33,** 1127–1132 (1999).

45. J. F. Schalles, F. R. Schiebe, P. J. Starks, and W. W. Troeger, "Estimation of algal and suspended sediment loads (singly and combined) using hyperspectral sensors and integrated meso-

cosm experiments," in *4th International Conference on Remote Sensing for Marine and Coastal Environments* (Environmental Research Institute of Michigan Ann Arbor, Mich., 1997), Vol. I, pp. 247–258.

46. J. F. Schalles, A. T. Sheil, J. F. Tycast, J. J. Alberts, and Y. Z. Yacobi, "Detection of chlorophyll, seston and dissolved organic matter in the estuarine mixing zone of Georgia coastal plain rivers," in *5th International Conference on Remote Sensing for Marine and Coastal Environments* (Environmental Research Institute of Michigan, Ann Arbor, Mich., 1998), Vol. II, pp. 315–324.

47. S. Tassan and G. M. Ferrari, "Proposal for the measurement of backward and total scattering by mineral particles suspended in water," Appl. Opt. **34,** 8345–8353 (1995).

48. J. Kromkamp and R. Wouts, "Particulate matter North Sea plus," Rep. NUSP 98-04 (Beleidscommissie Remote Sensing, Delft, The Netherlands, 1998).

49. G. Zibordi, V. Barale, G. M. Ferrari, N. Hoepffner, D. v. d. Linde, L. Alberotanza, P. Cova, and C. Ramasco, "Coastal atmosphere and sea time-series project (CoASTS)," in *Third International Conference on Remote Sensing for Marine and Coastal Environments* (Environmental Research Institute of Michigan, Ann Arbor, Mich., 1995), Vol. II, pp. 96–100.

50. R. P. Stumpf and J. R. Pennock, "Calibration of a general optical equation for remote sensing of suspended sediments in a moderately turbid estuary," J. Geophys. Res. **94,** 14,363–14,371 (1989).

51. R. J. Vos, M. Villars, J. N. Roozekrans, S. W. M. Peters, and W. v. Raaphorst, "RESTWAQ 2, Part 1. Integrated monitoring of total suspended matter in the Dutch coastal zone," Rep. NRSP-2 98-08 (Beleidscommissie Remote Sensing, Delft, The Netherlands, 1998).

52. I. J. A. Althuis and S. Shimwell, "Modelling of remote sensing reflectance spectra for suspended matter concentration detection in coastal waters," Adv. Remote Sens. **4,** 53–59 (1995).

53. A. G. Dekker, "Detection of water quality parameters for eutrophic waters by high resolution remote sensing," Ph.D. dissertation (Vrije Universiteit, Amsterdam, The Netherlands, 1993).

54. R. Doerffer, "Imaging spectroscopy for detection of chlorophyll and suspended matter," in *Imaging Spectroscopy: Fundamentals and Prospective Applications*, F. Toselli and J. Bodechtel, eds. (Kluwer Academic, Dordrecht, The Netherlands, 1991), pp. 215–257.

55. R. A. Neville and J. F. R. Gower, "Passive remote sensing of phytoplankton via chlorophyll *a* fluorescence," J. Geophys. Res. **82,** 3487–3493 (1977).

56. A. Bricaud, C. Roesler, and J. R. V. Zaneveld, "*In situ* methods for measuring the inherent optical properties of ocean waters," Limnol. Oceanogr. **40,** 393–410 (1995).

57. W. S. Pegau and J. R. V. Zaneveld, "Temperature-dependent absorption of water in the red and near-infrared portions of the spectrum," Limnol. Oceanogr. **38,** 188–192 (1993).

58. R. P. Bukata, J. H. Jerome, J. E. Bruton, S. C. Jain, and H. H. Zwick, "Optical water quality model of Lake Ontario. 1. Determination of the optical cross sections of organic and inorganic particulates in Lake Ontario," Appl. Opt. **20,** 1696–1703 (1981).

59. R. W. Gould, R. A. Arnone, and P. M. Martinolich, "Spectral dependence of the scattering coefficient in case 1 and case 2 waters," Appl. Opt. **38,** 2377–2383 (1999).

60. R. A. Barnes, A. W. Holmes, W. L. Barnes, W. E. Esaias, C. R. McClain, and T. Svitek, "SeaWIFS prelaunch radiometric calibration and spectral characterization," SeaWiFS Tech. Rep. 22, NASA Tech. Memo. 104566 (NASA, Greenbelt, Md., 1994).